

# Spin-exchange relaxation free magnetometry with Cs vapor

M. P. Ledbetter,\* I. M. Savukov, V. M. Acosta, and D. Budker†

*Department of Physics, University of California at Berkeley, Berkeley, California 94720-7300*

M. V. Romalis

*Department of Physics, Princeton University, Princeton, New Jersey, 08544*

(Dated: May 28, 2018)

We describe a Cs atomic magnetometer operating in the spin-exchange relaxation-free (SERF) regime. With a vapor cell temperature of 103°C we achieve intrinsic magnetic resonance widths  $\Delta B = 17 \mu\text{G}$  corresponding to an electron spin-relaxation rate of  $300 \text{ s}^{-1}$  when the spin-exchange rate is  $\Gamma_{SE} = 14000 \text{ s}^{-1}$ . We also observe an interesting narrowing effect due to diffusion. Signal-to-noise measurements yield a sensitivity of about  $400 \text{ pG}/\sqrt{\text{Hz}}$ . Based on photon shot noise, we project a sensitivity of  $40 \text{ pG}/\sqrt{\text{Hz}}$ . A theoretical optimization of the magnetometer indicates sensitivities on the order of  $2 \text{ pG}/\sqrt{\text{Hz}}$  should be achievable in a  $1 \text{ cm}^3$  volume. Because Cs has a higher saturated vapor pressure than other alkali metals, SERF magnetometers using Cs atoms are particularly attractive in applications requiring lower temperatures.

PACS numbers: PACS. 07.55.Ge, 32.80.Bx, 42.65.-k

## I. INTRODUCTION

Sensitive atomic magnetometers have recently found application in the field of magnetic resonance imaging [1], magneto-encephalography [2], and searches for physics beyond the standard model [3]. A recent review may be found in Ref. [4]. The most sensitive atomic magnetometers presently are the spin-exchange relaxation free (SERF) magnetometers [5] in which relaxation due to spin-exchange collisions is eliminated by operating in the regime where the spin-exchange rate is much greater than the rate of Larmor precession [6, 7]. In Ref. [5], sensitivity of  $5 \text{ pG}/\sqrt{\text{Hz}}$  was achieved with the cell operating at 190°C using potassium atoms. Estimates of the fundamental sensitivity limit of such magnetometers are several orders of magnitude better for a  $1 \text{ cm}^3$  volume and scale as the square-root of the spin-destruction cross section.

Here we demonstrate operation of a Cs magnetometer in the SERF regime, achieving a sensitivity of about  $400 \text{ pG}/\sqrt{\text{Hz}}$  with a vapor cell temperature of only 103°C. The overlapping volume of the pump and probe beams is about  $0.02 \text{ cm}^3$ , but the effective volume, determined by diffusion, is about  $1 \text{ cm}^3$ . Based on optical rotation measurements, the projected photon shot noise limit for our experimental conditions is about  $40 \text{ pG}/\sqrt{\text{Hz}}$ . The spin-destruction cross section for Cs is  $\sigma_{SD} = 2 \times 10^{-16} \text{ cm}^2$ , about 200 times larger than for K [8]. Hence, the fundamental sensitivity of a Cs SERF magnetometer should be roughly a factor of 14 worse than one based on K. However, it is often the case that environmental noise due to, for example, Johnson currents in magnetic shields is far larger than atomic shot noise,

and hence little is lost by using Cs. One of the primary motivations for investigating Cs in the SERF regime is the fact that it has the highest saturated vapor pressure of all the stable alkalis, yielding significantly lower operating temperatures. This opens up the possibility of operating in the SERF regime with paraffin coated cells, of interest due to the lower light power requirements in evacuated cells. The low temperature aspect of Cs is also attractive for applications such as NMR measurements with liquids in microfluidic channels, which is expected to be an important measurement modality in future “lab-on-a-chip” devices [9].

## II. BLOCH EQUATIONS

A full treatment of the system requires the use of density matrix theory (see, for example, Ref [10]). However, the description can be greatly simplified when the spin-exchange rate

$$\Gamma_{SE} = T_{SE}^{-1} = n\sigma_{SE}\bar{v} \quad (1)$$

(here  $n$  is the alkali number density,  $\sigma_{SE} \approx 2 \times 10^{-14} \text{ cm}^2$  is the spin-exchange cross section, and  $\bar{v}$  is the average relative velocity of the colliding alkali atoms) is much faster than precession in the magnetic field,  $\Gamma_{SE} \gg g_s\mu_B B/(2I+1)$ . Here  $g_s \approx 2$  is the electron Landé factor,  $\mu_B$  is the Bohr magneton,  $B$  is the magnitude of an applied magnetic field, and  $I$  is the nuclear spin. In this case the density matrix assumes a spin-temperature distribution and the ground state can be well described by Bloch equations for the electron spin polarization  $\mathbf{P} = \langle \mathbf{S} \rangle / S$  [11, 12, 13]:

$$\frac{d\mathbf{P}}{dt} = \frac{1}{q(P)} \times \left( g_s\mu_B \mathbf{P} \times \mathbf{B} + R(\mathbf{s} - \mathbf{P}) - \frac{\mathbf{P}}{T_1, T_2} - \Gamma_{pr}\mathbf{P} \right). \quad (2)$$

\*Electronic address: ledbetter@berkeley.edu

†Electronic address: budker@berkeley.edu

Here  $\mathbf{s}$  is the optical pumping vector along the direction of propagation of the pump with magnitude equal to the degree of circular polarization,  $R$  is the optical pumping rate due to the pump beam, and  $\Gamma_{pr}$  is the rate of depolarization due to the linearly polarized probe beam. The quantity  $q(P)$  is the nuclear slowing-down factor, which for nuclear spin  $I = 7/2$ , is [14]

$$q(P) = \frac{2(P^6 + 17P^4 + 35P^2 + 11)}{P^6 + 7P^4 + 7P^2 + 1}. \quad (3)$$

In the low polarization limit  $q(0) = 22$ , while in the high polarization limit,  $q(1) = 8$ . The latter limit, when all atoms are pumped into the stretched state, corresponds to the slowing down factor for nuclear spin  $I = 7/2$  in the absence of spin-exchange collisions  $q = 2I + 1 = 8$ . In Eq. (2),  $T_1$  and  $T_2$  are the longitudinal and transverse (with respect to  $\mathbf{B}$ ) relaxation times, respectively. The transverse relaxation time can be written

$$\frac{1}{T_2} = \Gamma_{SD} + \frac{1}{T_2^{SE}}, \quad (4)$$

where  $\Gamma_{SD}$  is the electron spin-destruction rate and  $(T_2^{SE})^{-1}$  is the contribution to relaxation from spin-exchange collisions. For low polarizations and small magnetic fields, relaxation due to spin-exchange is quadratic in the magnetic field [7]

$$\frac{1}{T_2^{SE}} = \frac{\Omega_0^2}{\Gamma_{SE}} \frac{q(0)^2 - (2I + 1)^2}{2}, \quad (5)$$

where  $\Omega_0 = Bg_s\mu_B/q(0)$ .

In some of the measurements described below, small, quasistatic magnetic fields are applied, and the conditions are such that relaxation due to spin-exchange collisions can be ignored. In our present experimental setup (see Fig. 1) optical pumping is along the  $z$  axis (the longitudinal direction) and optical rotation of the probe is due to  $P_x$ . The steady state solutions to Eq. (2) can be found by setting the L.H.S. to zero, resulting in

$$P_x = P_0 \frac{B_x B_z - B_y \Delta B}{B^2 + \Delta B^2}, \quad (6)$$

$$P_z = P_0 \frac{B_z^2 + \Delta B^2}{B^2 + \Delta B^2}, \quad (7)$$

where

$$\Delta B = (R + \Gamma_{pr} + \Gamma_{SD})/g_s\mu_B, \quad (8)$$

$$P_0 = sR/(R + \Gamma_{pr} + \Gamma_{SD}). \quad (9)$$

Note that Eqs. (6)-(9) are independent of the nuclear spin.

To study the effects of spin exchange, we find it convenient to apply a small rotating field  $\hat{\mathbf{x}}B_1 \sin \omega t + \hat{\mathbf{y}}B_1 \cos \omega t$  in the presence of a larger bias field  $B_z$ . In this case we find the in-phase and quadrature components

of  $P_x$

$$P_x^{(in)} = -P_0 \frac{g_s\mu_B B_1}{q(P)} \frac{\Delta\omega}{(\omega - \Omega_0)^2 + \Delta\omega^2}, \quad (10)$$

$$P_x^{(out)} = -P_0 \frac{g_s\mu_B B_1}{q(P)} \frac{\omega - \Omega_0}{(\omega - \Omega_0)^2 + \Delta\omega^2}, \quad (11)$$

where  $\Delta\omega = (R + \Gamma_{pr} + \Gamma_{SD} + 1/T_2^{SE})/q(P)$ .

In the presence of rapid quenching of the excited state by  $N_2$ , the effects of optical pumping and the optical properties of the medium can be treated with an effective ground state formalism [15]. When the pressure broadened optical width is much larger than the hyperfine splitting, the optical pumping rate for light of frequency  $\nu$  is given by [16]

$$R = \Phi\sigma = \Phi r_e c f \frac{\Delta\nu/2}{(\Delta\nu/2)^2 + (\nu - \nu_0)^2}, \quad (12)$$

where  $\sigma$  is the absorption cross section,  $r_e = 2.8 \times 10^{-13}$  cm is the classical radius of the electron,  $c$  is the speed of light,  $f$  is the oscillator strength (roughly 1/3 for D1 light and 2/3 for D2 light),  $\Phi$  is the photon flux per unit area and  $\Delta\nu$  is the full-width at half-maximum of the optical transition of frequency  $\nu_0$ . Optical rotation of linearly polarized D2 light, propagating in the  $x$  direction is dispersive in the detuning of the probe beam from optical resonance [15, 17],

$$\phi = \frac{1}{4} l r_e c f n P_x D(\nu), \quad (13)$$

where  $l$  is the optical path length and  $D(\nu) = (\nu - \nu_0)/[(\nu - \nu_0)^2 + (\Delta\nu/2)^2]$ .

### III. EXPERIMENTAL SETUP AND PROCEDURE

The experimental setup is shown in Fig. 1. A glass cell containing a droplet of Cs metal, 600 Torr He buffer gas (to reduce the rate at which atoms in the central part of the cell diffuse to the cell walls) and 20 Torr of  $N_2$  (to eliminate radiation trapping and improve optical pumping efficiency) is placed inside a four-layer set of magnetic shields. The cell has a roughly cubic profile, about 2 cm on a side. After degaussing, the residual fields inside the magnetic shields are on the order of 2–3  $\mu$ G. From the known rates of pressure broadening of Cs lines by helium [18], we extrapolate the FWHM of the D1 and D2 optical resonances to be  $\Delta\nu = 15.7$  and 14.1 GHz, respectively. The cell was heated to 103°C by flowing hot air through the space between the walls of a double-wall oven. The oven was designed so that the optical path was unperturbed by the flowing air. At 103°C, the saturated Cs vapor concentration is about  $[Cs] = 1.7 \times 10^{13}$  cm $^{-3}$ . Optical pumping was accomplished by circularly polarized laser light propagating in the  $z$  direction tuned to the center of the Cs D1 line (the exact tuning was chosen to minimize light shifts). The pump beam was about

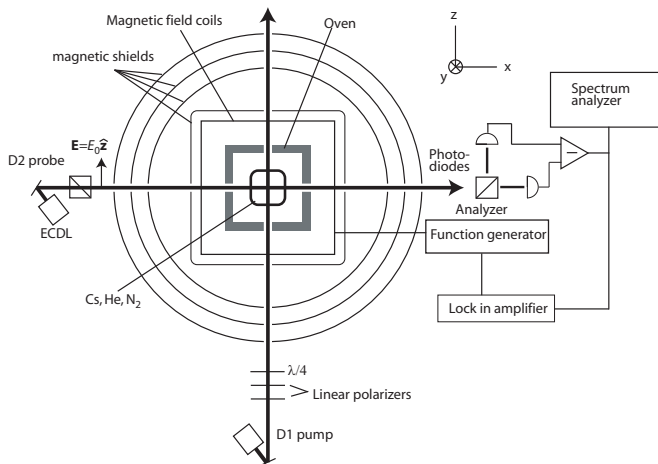


FIG. 1: Experimental setup. A four-layer magnetic shield provides a magnetically shielded environment. Circularly polarized light tuned to the D1 line, propagating in the  $z$  direction produces ground state orientation in the  $z$  direction. The  $x$  component of orientation  $S_x$  is detected via optical rotation of linearly polarized light, tuned to the D2 line, propagating in the  $x$  direction.

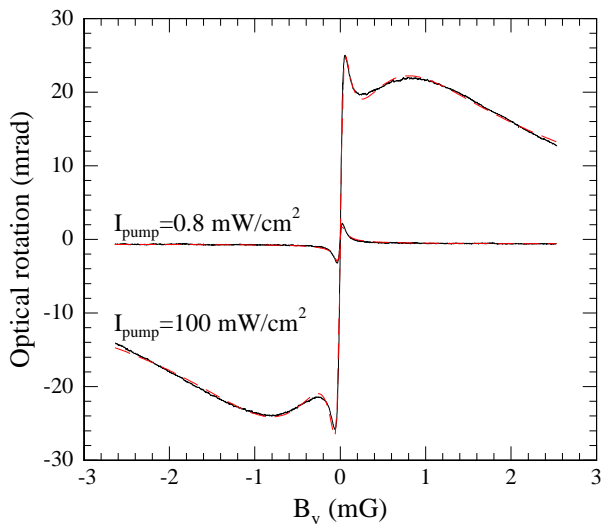


FIG. 2: Optical rotation (solid line) of a weak ( $\approx 0.5 \text{ mW/cm}^2$ ) probe beam as a function of  $B_y$  for pump intensities as indicated next to each trace. The dashed lines are fits to one or two dispersive Lorentzians, as described in the text.

4 mm in diameter. A linearly polarized probe beam, with cross section  $\approx 2 \times 3 \text{ mm}^2$ , tuned about 5 optical linewidths from the center of the pressure broadened D2 line (where signal was maximized) propagated in the  $x$  direction through the cell. Note that based on Eq. (13), one expects the maximum optical rotation to occur for detuning from resonance by  $\Delta\nu/2$ . However, the signal is the product of the transmission and optical rotation, and since there are many optical depths in our cell (on

resonance, 1 cm corresponds to about 12 optical depths under the conditions of our measurements), it was necessary to detune far from resonance. Circular birefringence of the medium proportional to  $P_x$  rotates the polarization of the probe beam, which is analyzed after the cell with a balanced polarimeter. To investigate the zero-field resonance, where behavior is described by Eq. (6), optical rotation of the probe beam was measured as a function of a static field  $B_y$  for all other fields zeroed.  $B_x$  ( $B_z$ ) can be zeroed by making use of Eq. (6): a small, slowly oscillating field ( $B_x$ )  $B_z$  is applied while  $B_x$  ( $B_z$ ) is adjusted until the resulting signal is zero. To study the effects of spin-exchange broadening at non-zero fields, optical rotation was detected synchronously using a lock-in amplifier while a small rotating magnetic field  $\hat{y}B_1 \cos \omega t + \hat{x}B_1 \sin \omega t$  was applied in the presence of a larger bias field  $B_z$ .

## IV. EXPERIMENTAL RESULTS AND DISCUSSION

### A. Zero-field resonance

In Fig. 2 the solid curves show the magneto-optical rotation of a weak probe beam ( $I_{pr} \approx 0.5 \text{ mW/cm}^2$ ) as a function of magnetic field  $B_y$  for two different pump intensities. The dashed line overlaying the data for weak pump light,  $I_{pump} = 0.8 \text{ mW/cm}^2$ , is a fit based on Eq. (6) with  $\Delta B = 23 \mu\text{G}$ . For more intense pump light  $I_{pump} = 100 \text{ mW/cm}^2$ , the optical rotation is well described by the sum of two dispersive Lorentzians with widths  $\Delta B = 56 \mu\text{G}$  and  $\Delta B = 940 \mu\text{G}$ , as indicated by the dashed red line. In Fig. 3 we plot the width and peak-to-peak amplitude of the optical rotation for the single feature observed for pump intensities below about  $15 \text{ mW/cm}^2$  (stars) and for the nested features observed at higher pump intensities (squares and triangles). In either regime, the width is linear in light intensity. When the two features become resolved, the amplitude of the broad resonance appears saturated, while the amplitude of the narrow resonance continues to grow, approaching saturation at the highest light power.

The difference in the behavior of magneto-optical rotation for low and high pump intensities is essentially due to diffusion of atoms into and out of the pump beam, creating two regions with differing polarization and rates of power broadening. Similar narrowing effects due to diffusion have been observed in the context of electromagnetically induced transparency in buffer gas cells [20]. Nested resonances have also been observed in the context of non-linear magneto-optical rotation in paraffin coated cells [21]. In a simplified model, the cell can be divided into regions illuminated and dark with respect to the pump beam. The optical pumping rate  $R$  inside the pump beam is determined by Eq. (12) so that the power broadened width and polarization of atoms inside the pump beam is given by Eqs. (8) and (9). The region outside the

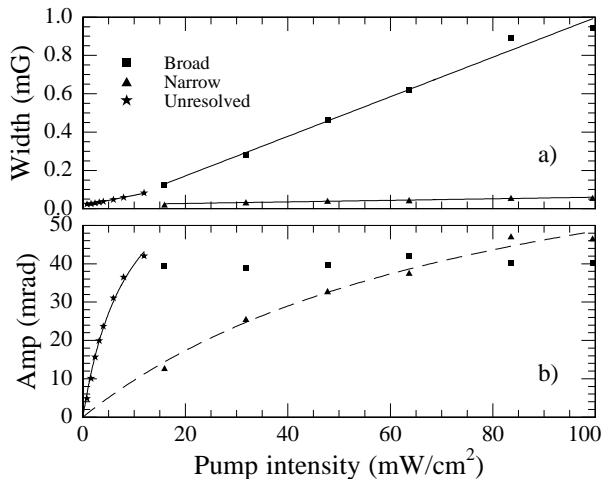


FIG. 3: Zero-field resonance half-width at half-max (top panel) and peak-to-peak amplitude (bottom panel) as a function of pump power. The lines overlaying the data are fits described in the text.

pump beam is polarized via diffusion and hence the average optical pumping rate is suppressed by the ratio  $\Gamma_{SD}/(\Gamma_{SD} + \Gamma_D)$ , where  $\Gamma_D$  is the rate of diffusion of atoms into and out of the pump beam. Hence the width of the zero field resonance and polarization for atoms outside the pump beam is

$$\Delta B^{out} = \frac{1}{g_s \mu_B} \left( R \frac{\Gamma_{SD}}{\Gamma_{SD} + \Gamma_D} + \Gamma_{SD} \right), \quad (14)$$

$$P_0^{out} = \frac{R}{R + \Gamma_D + \Gamma_{SD}}. \quad (15)$$

For pump intensities such that  $R$  is small compared to  $\Gamma_{SD}$  the width of the resonance due to atoms inside and outside of the pump beam is determined primarily by  $\Gamma_{SD}$  and hence a single feature is visible. The polarization of the region outside the pump beam is smaller than inside the pump beam by a factor  $\Gamma_{SD}/(\Gamma_{SD} + \Gamma_D)$  and hence the amplitude of optical rotation is dominated by the region inside the pump beam. When the optical pumping rate inside the beam is large compared to  $\Gamma_{SD}$ , the region inside the pump beam becomes saturated and optical rotation is sufficiently broadened so that the smaller narrow feature due to the region outside the pump beam becomes distinguishable. As  $R$  becomes large compared to  $\Gamma_D + \Gamma_{SD}$ , the region outside the pump beam becomes fully polarized and optical rotation approaches an asymptote.

Overlaying the data in Fig. 3a are linear fits based on Eq. (8) with  $R = \eta I_{pump}$ . The fit to the low pump intensity data yields  $\eta = 93 \text{ s}^{-1}/(\text{mW}/\text{cm}^2)$  and zero light-power width  $\Delta B_0 = 17 \pm 3 \mu\text{G}$  corresponding to  $\Gamma_{SD} = 300 \pm 52 \text{ s}^{-1}$ . This can be compared to the expected spin-destruction rate based on previous measure-

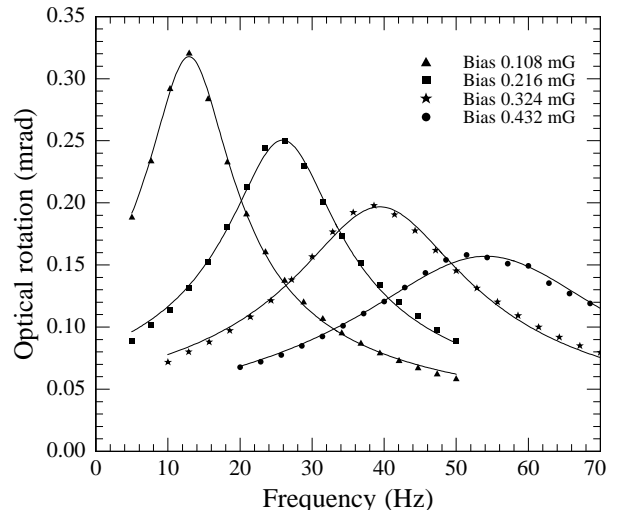


FIG. 4: Response of magnetometer to a small rotating magnetic field of magnitude  $B_1 = 0.55 \mu\text{G}$  transverse to a larger bias field  $B_z$  for several different values of  $B_z$ . For these data the pump and probe intensities were  $4 \text{ mW}/\text{cm}^2$  and  $1.3 \text{ mW}/\text{cm}^2$  respectively.

ments of the spin-destruction cross sections

$$\Gamma_{SD} = [\text{Cs}] \bar{v}^{\text{Cs}} \sigma_{SD}^{\text{Cs}} + [\text{He}] \bar{v}^{\text{He}} \sigma_{SD}^{\text{He}} + [\text{N}_2] \bar{v}^{\text{N}_2} \sigma_{SD}^{\text{N}_2}. \quad (16)$$

Here,  $\sigma_{SD}^{\text{Cs}} = 2 \times 10^{-16} \text{ cm}^2$  [8],  $\sigma_{SD}^{\text{He}} = 3 \times 10^{-23} \text{ cm}^2$  [19], and  $\sigma_{SD}^{\text{N}_2} = 6 \times 10^{-22} \text{ cm}^2$  [19] are the spin destruction cross sections for Cs-Cs, Cs-He and Cs-N<sub>2</sub> collisions respectively. The mean relative velocity  $\bar{v}^X$  differs between colliding pairs, and hence the superscript in Eq. (16). The contributions to the spin-destruction rate from Cs, He and N<sub>2</sub> collisions are  $119 \text{ s}^{-1}$ ,  $88 \text{ s}^{-1}$  and  $32 \text{ s}^{-1}$  respectively yielding a total spin destruction rate  $\Gamma_{SD} = 240 \text{ s}^{-1}$ , in reasonable agreement with the present measurements.

In Fig. 3b, the solid line overlaying the amplitude of the zero-field resonance for low pump intensity is a fit to  $a\eta I/(\eta I + \Gamma_{SD})$  with  $\Gamma_{SD}$  fixed by the value determined above, yielding  $a = 75 \text{ mrad}$  and  $\eta = 33 \text{ s}^{-1}/(\text{mW}/\text{cm}^2)$ , about a factor of 3 smaller than the pump rate determined from the broadening. The reason for the difference in pump rates determined from the amplitude and the rate of broadening is due to diffusion as discussed above: The pump rate determined by the broadening will be dominated by the illuminated region, while the pump rate determined from the amplitude represents an average pump rate over the volume the polarized atoms occupy during the course of one relaxation period.

## B. Spin-exchange effects

To explore the effects of spin-exchange on transverse relaxation we apply a bias magnetic field in the  $z$  di-

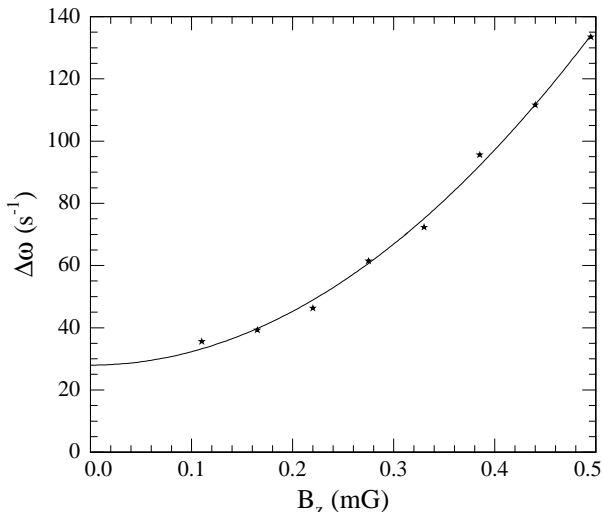


FIG. 5: Half-width at half-maximum of the bias-field resonances shown in Fig. 4 as a function of magnetic field.

rection (along the pump beam) and a small transverse rotating magnetic field to excite a component of polarization transverse to the bias field. In-phase and quadrature components of the resulting optical rotation signal are detected synchronously using a lock-in amplifier. In Fig. 4 we show the quadrature sum of the in- and out- of phase optical rotation signals as a function of frequency for several different values of the bias magnetic field. Overlaying the data are fits to  $a\Delta\omega/\sqrt{(\omega - \Omega_0)^2 + \Delta\omega^2}$  (see Eqs. (10) and (11)). For these data, the pump and probe intensities were about 4 and 1.3 mW/cm<sup>2</sup>, respectively. Based on the data shown in Fig. 3, these intensities produce power broadening by about a factor of 2 over the zero light-power width, however the slowing down factor, determined from a linear fit to  $\Omega_0$ , was very nearly  $q = 22$  indicating that the polarization was quite low (see Eq. (3)).

In Fig. 5 we plot the half-width at half-maximum  $\Delta\omega$  of the resonances shown in Fig. 4 as a function of the bias field. Overlaying the data is a fit based on Eq. (5) with  $\Delta\omega = (q(0)T_2)^{-1}$  and  $\Omega_0 = g_s\mu_B B/q(0)$ , allowing for a constant offset due to spin-destruction collisions, diffusion and power broadening, yielding a spin-exchange rate  $\Gamma_{SE} = 14300 \pm 350 \text{ s}^{-1}$ . For  $n = 1.7 \times 10^{13} \text{ cm}^{-3}$  obtained from the saturated vapor pressure curve, Eq. (1) gives a spin-exchange rate of about  $12000 \text{ s}^{-1}$ . Temperature fluctuations of 2 or 3 degrees could cause significant variations in the vapor pressure, and hence we consider this reasonable agreement with measurements of spin-exchange broadening.

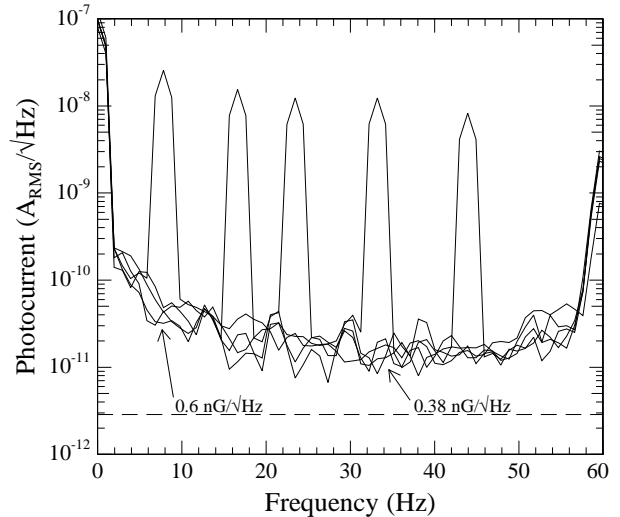


FIG. 6: Fourier transform of magnetometer signal (solid lines) with calibration peaks of amplitude  $B_1 = 0.55 \mu\text{G}$  applied at several different frequencies. The dashed line represents photon shot noise.

### C. Sensitivity

We evaluate the performance of the magnetometer by monitoring the noise level at the output of the balanced polarimeter using a Stanford Research Systems SR770 spectrum analyzer. To calibrate the magnetometer, we apply a small oscillating field  $B_y = B_1 \cos\omega t$  with  $B_1 = 0.55 \mu\text{G}$  at several different frequencies. The resulting spectra are shown as solid lines in Fig. 6. The triangular shape of the calibration peaks is due to the use of the built in Hann windowing function with coarse spectral resolution. For these data, the pump and probe intensities were 100 mW/cm<sup>2</sup> and 4 mW/cm<sup>2</sup>, respectively, and all three components of the DC magnetic field have been zeroed. The sensitivity, in  $\text{G}_{\text{RMS}}/\sqrt{\text{Hz}}$  is determined by  $\delta B = B_1/(\sqrt{2}S/N)$  yielding a sensitivity of about 400  $\text{pG}_{\text{RMS}}/\sqrt{\text{Hz}}$  at 30 Hz and about 600  $\text{pG}_{\text{RMS}}/\sqrt{\text{Hz}}$  at 10 Hz. When the pump beam was blocked, effectively turning the magnetometer off, noise at low frequencies dropped by about a factor of 5. The excess noise could be due to real fluctuations of the ambient field (either due to imperfect magnetic shielding or noise in the current source), or due to fluctuations in the pump power coupled with misalignment of the pump and probe beams. The dashed line in Fig. 6 represents the estimated photon shot noise limit in the difference of the photocurrents for unit bandwidth,  $\delta I = \sqrt{4eI}$  where  $I$  is the photocurrent in one channel of the balanced polarimeter, yielding a photon shot noise limited sensitivity of about 40  $\text{pG}/\sqrt{\text{Hz}}$  at 10 Hz. Optimization of geometry to maximize the overlapping volumes of the pump and probe beams will likely yield improvements in the photon shot noise limit.

## V. CONCLUSIONS

We demonstrated a Cs atomic magnetometer in the spin-exchange relaxation free regime. The primary advantage of using Cs is the ability to work at lower temperatures. Future work with atomic magnetometers in the context of microfluidic NMR will make use of this feature. At 103°C we realized magneto-optical rotation features with intrinsic linewidths of 17  $\mu\text{G}$  corresponding to a relaxation rate of about 300  $\text{s}^{-1}$  when the spin-exchange rate was about  $\Gamma_{SE} = 14000 \text{ s}^{-1}$ . We achieved a sensitivity of 400 pG/ $\sqrt{\text{Hz}}$ . Based on estimates of the photon shot noise, we project a sensitivity of about 40 pG/ $\sqrt{\text{Hz}}$ . We suspect that the demonstrated sensitivity was limited by pump laser noise and ambient magnetic field noise. Theoretical optimization of the magnetometer (presented in the Appendix below) indicates it should be possible to achieve sensitivity on the order of 2 pG/ $\sqrt{\text{Hz}}$  in a 1  $\text{cm}^{-3}$  volume. We believe the primary reason for falling short of this level is suboptimal geometry (probe beam cross section was only  $2 \times 3 \text{ mm}^2$ ) detuning and light power of both pump and probe. This work was supported by an ONR MURI grant.

## VI. APPENDIX: THEORETICAL OPTIMIZATION

We now present a theoretical optimization of the magnetometer, maximizing sensitivity to small, quasistatic fields. The analysis is similar to Refs. [22] and [23], in that spin-projection noise and photon shot noise are considered independently (noise due to light shifts is not considered, because in principle, it can be eliminated by orthogonality of pump and probe beams [23]). Spin-projection noise is typically written as

$$\delta B \approx \frac{1}{\gamma\sqrt{NtT_2}}, \quad (17)$$

where  $\gamma$  is the gyromagnetic ratio,  $N$  is the number of atoms,  $t$  is the measurement time and  $T_2$  is the transverse relaxation time. In the SERF regime  $T_2 = q(P)/\Gamma_{SD}$  and  $\gamma = g_s\mu_B/q(P)$  both depend on the nuclear slowing down factor. Inserting these expressions into Eq. (17), one might conclude that the atomic shot noise limit scales as  $\sqrt{q(P)}$ . However, it turns out that the nuclear slowing down factor drops out of the problem. The reasons are somewhat subtle, so we go into some detail.

Spin-projection noise arises (in the present geometry) due to uncertainty in the  $x$  component of angular momentum  $F_x$ , defined as  $\Delta F_x = \sqrt{\langle F_x^2 \rangle - \langle F_x \rangle^2}$ . For a spin temperature distribution with polarization in the  $z$  direction,  $\rho \propto e^{\beta F_z}$ , where  $\beta = \ln(1+P)/(1-P)$  is the spin temperature parameter [10],  $\langle F_x \rangle = 0$ . Thus  $\Delta F_x = \sqrt{\text{Tr}(\rho F_x^2)}$ . Evaluation of this trace results in  $\Delta F_x(P) = \sqrt{q(P)/4}$  per atom with  $\rho$  normalized so that  $\text{Tr}\rho = 1$ . Assuming that  $N = nV$  uncorrelated atoms

are involved in the measurement, the ensemble averaged uncertainty scales as  $1/\sqrt{nV}$ ,

$$\delta F_x(P) = \sqrt{\frac{q(P)}{4nV}}. \quad (18)$$

In the large polarization limit,  $\delta F_x(1) = \sqrt{2/nV}$ . This limit can be obtained from the angular momentum commutation relations  $[F_x, F_y] = iF_z$  which yield the minimum uncertainty  $\sqrt{|\langle F_z \rangle|/2}$ . If all the atoms are in the stretched state, corresponding to  $P = 1$ ,  $\langle F_z \rangle = 4$ , we have, again assuming uncorrelated atoms,  $\delta F_x = \sqrt{2/nV}$ . The uncertainty in the low polarization limit is somewhat larger,  $\delta F_x(0) = \sqrt{11/2nV}$ . This limit can also be verified by noting that for an unpolarized sample  $\rho = \mathbf{1}/(2S+1)(2I+1)$  and  $\text{Tr}(\rho F_x^2) = \text{Tr}(\rho F_z^2)$ . As an aside, we note that the reduction in uncertainty  $\delta F_x$  with increasing polarization only occurs for angular momentum greater than  $1/2$ .

After measuring continuously for time  $t$  long compared to the lifetime of the polarization,  $q(P)/(R + \Gamma_{pr} + \Gamma_{SD})$ , the uncertainty is [22, 24]

$$\langle \delta F_x \rangle_t = \delta F_x \sqrt{\frac{2q(P)}{(R + \Gamma_{pr} + \Gamma_{SD})t}} \quad (19)$$

$$= \frac{q(P)}{\sqrt{2t(R + \Gamma_{pr} + \Gamma_{SD})nV}}. \quad (20)$$

In a spin-temperature distribution, the ratio of the total angular momentum to that stored in the electron is given by  $q(P)$ ,  $\langle \mathbf{F} \rangle = (q(P)/2)\mathbf{P}$  [10] and thus

$$\delta P_x = \frac{2}{q(P)} \langle \delta F_x \rangle_t = \sqrt{\frac{2}{t(R + \Gamma_{pr} + \Gamma_{SD})nV}}. \quad (21)$$

From Eq. (6), we find for all fields zeroed, that the uncertainty  $\delta B_y$  in a measurement of  $B_y$  is related to fluctuations of  $P_x$  by

$$\delta B_y = \frac{R + \Gamma_{pr} + \Gamma_{SD}}{g_s\mu_B} \frac{\delta P_x}{P_z}. \quad (22)$$

Inserting Eq. (21) into Eq. (22) we find that the spin-projection noise is

$$\delta B_{spn} = \frac{1}{g_s\mu_B P_z} \sqrt{\frac{2(R + \Gamma_{pr} + \Gamma_{SD})}{nVt}}, \quad (23)$$

It is interesting to note that this result is independent of any nuclear slowing-down factors. Neglecting broadening due to the probe beam, the minimum value of spin-projection noise

$$\delta B_{spn}^{min} = \frac{3}{g_s\mu_B} \sqrt{\frac{3\Gamma_{SD}}{2nVt}} \quad (24)$$

is obtained when  $R = 2\Gamma_{SD}$ .

We now address photon shot noise. To simplify the analysis, we assume that the volume  $V$  occupied by the sample is a cube with sides of length  $l$ , fully illuminated by both pump and probe. If the probe beam is detuned far from resonance so that the medium is optically thin, optical rotation drops slowly, scaling as  $D(\nu) \approx 1/(\nu - \nu_0)$ , compared to absorption which scales as  $1/(\nu - \nu_0)^2$ , a very favorable situation. In this case, photon shot noise in the optical rotation angle is given by  $\delta\phi = 1/2\sqrt{\Phi_0 l^2 t}$  where  $\Phi_0$  is the probe photon intensity and  $l^2$  is the cross section of the probe beam. Combining this with Eqs. (13) and (22), the photon shot noise contribution to magnetic field sensitivity is

$$\delta B_{psn} = \frac{1}{g_s \mu_B P_z} \frac{2(R + \Gamma_{pr} + \Gamma_{SD})}{lr_e c f n D(\nu) \sqrt{\Phi_0 l^2 t}}. \quad (25)$$

This can be rearranged

$$\delta B_{psn} = \frac{1}{g_s \mu_B P_z \sqrt{n V t}} \frac{2(R + \Gamma_{pr} + \Gamma_{SD})}{\sqrt{\Gamma_{pr} \text{OD}_0}}, \quad (26)$$

where  $\text{OD}_0 = 2r_e c f n l / \Delta\nu$  is the optical depth on resonance and

$$\Gamma_{pr} = \Phi_0 r_e c f \frac{\Delta\nu/2}{(\nu - \nu_0)^2} \quad (27)$$

is the probe rate for far detuned light.

Adding spin-projection noise Eq. (23) and photon shot noise Eq. (26) in quadrature, yields

$$\delta B = \frac{1}{g_s \mu_B P_z \sqrt{n V t}} \times \sqrt{2(R + \Gamma_{pr} + \Gamma_{SD}) + \frac{4(R + \Gamma_{pr} + \Gamma_{SD})^2}{\Gamma_{pr} \text{OD}_0}}. \quad (28)$$

Inspection of Eq. (28) shows that the probe pump rate can be increased until  $\Gamma_{pr} \approx \Gamma_{SD}$  without significant increase to either spin-projection noise or photon shot noise. If the resonant optical depth  $\text{OD}_0$  is sufficiently large, the contribution from photon shot noise becomes

negligible. In the limit of infinite resonant optical depth Eq. (28) is optimized for  $R = 4\Gamma_{SD}$  and  $\Gamma_{pr} = \Gamma_{SD}$  so that

$$\delta B_{opt} = \frac{3\sqrt{3}}{g_s \mu_B} \sqrt{\frac{\Gamma_{SD}}{n V t}}. \quad (29)$$

For a volume of  $1 \text{ cm}^3$  and a density of  $n = 1.7 \times 10^{13} \text{ cm}^{-3}$ , and spin-destruction rate  $\Gamma_{SD} = 300 \text{ s}^{-1}$  obtained in the experiment at  $103^\circ\text{C}$ , this expression evaluates to about  $1.7 \text{ pG}/\sqrt{\text{Hz}}$ , where we have assumed that a bandwidth of  $1 \text{ Hz}$  corresponds to a measurement time of  $0.5 \text{ s}$ . In the experiment, spin-destruction collisions due to alkali-alkali collisions accounted for only about  $1/3$  of the total spin-destruction rate, so somewhat higher sensitivities may be achieved by operating at higher temperatures where alkali-alkali collisions dominate the spin-destruction rate.

The above analysis indicates that optimal sensitivity is achieved when the probe is tuned sufficiently far from resonance so that the medium is optically thin, minimizing photon shot noise. Practical limitations such as finite light power will limit how far one can detune from resonance. Dropping the assumption of large probe detuning one finds, for the parameters described above and probe light tuned 3 optical linewidths away from resonance so that the optical depth is about  $1/3$ , that the sensitivity is roughly a factor of 2 larger than the spin-projection noise limit. Of course, technical sources of noise due to, e.g. vibrations or air currents, are often much larger than photon shot noise. In this case, it is desirable to tune the laser closer to optical resonance so that the optical rotation due to small magnetic fields is larger than other sources of noise. Finally, we note that the optimal tuning of the probe light depends on the particulars of the probing scheme. For example, Ref. [25] considers the case of nonlinear magneto-optical rotation, where optimal sensitivity is achieved when the probe is tuned so that there is roughly one optical depth. The primary reason for the difference is that optical rotation in that case scales (similarly to absorption) as the inverse square of the detuning.

- 
- [1] S. Xu *et al.* Proc. Nat. Acad. Sci, 10.1073/pnas.0605396103 (2006).
  - [2] H. Xia, A. B. Baranga, D. Hoffman, and M. V. Romalis. Appl. Phys. Lett. 89, 211104 (2006).
  - [3] D. Bear, R. E. Stoner, R. L. Walsworth, V. A. Kostelecky, and C. D. Lane, Phys. Rev. Lett. **85**, 5038 (2000); Phys. Rev. Lett. **89**, 209902(E) (2002).
  - [4] D. Budker and M. V. Romalis, Nature Physics **3**, 227 (2007).
  - [5] I. K. Kominis, T. W. Kornack, J. C. Allred, and M. V. Romalis, Nature **422**, 596 (2003).
  - [6] W. Happer and H. Tang, Phys. Rev. Lett. **31**, 273 (1973).
  - [7] W. Happer and A. C. Tam, Phys. Rev. A **16**, 1877 (1977).
  - [8] N.D. Bhaskar, J. Pietras, J. Camparo, W. Happer and J. Liran, Phys. Rev. Lett **44**, 930 (1980).
  - [9] V. Shah, S. Knappe, J. Kitching, M.P. Ledbetter, D. Budker, I. M. Savukov S. Xu, D. Michalak and A. Pines, *et al* to be published.
  - [10] S. Appelt *et al.* Phys. Rev. A **58**, 1412 (1998).
  - [11] J.C. Allred, R.N. Lyman, T.W. Kornack, and M.V. Romalis, Phys. Rev. Lett. **89**, 130801 (2002).
  - [12] T.W. Kornack and M.V. Romalis, Phys. Rev. Lett., **89**, 253002 (2002).
  - [13] S.J. Seltzer and M.V. Romalis, Appl. Phys. Lett **85**, 4804 (2004).
  - [14] I.M. Savukov and M.V. Romalis, Phys. Rev. A, **71**,

- 023405 (2005).
- [15] W. Happer and B. Mathur, Phys. Rev. **163**, 12 (1967).
  - [16] S. Appelt, A. B. Baranga, A. R. Young and W. Happer Phys. Rev. A **59**, 2078 (1999).
  - [17] T. W. Kornack, Ph.D. Thesis, Princeton University, 2005.
  - [18] A. Andalkar and R. B. Warrington Phys. Rev. A **65**, 032708 (2002).
  - [19] N. Beverini, P. Minguzzi, and F. Strumia, Phys. Rev. A **4**, 550 (1971).
  - [20] Y. Xiao, I. Novikova, D. F. Phillips and R. L. Walsworth, Phys. Rev. Lett. **96** 043601 (2006).
  - [21] D. Budker, V. Yashchuk and M. Zolotarev, Phys. Rev. Lett. **81**, 5788 (1998).
  - [22] I.M. Savukov, S.J. Seltzer, M.V. Romalis, and K.L. Sauer, Phys. Rev. Lett. **95**, 063004 (2005).
  - [23] M. Auzinsh *et al.* Phys. Rev. Lett. **93**, 173002 (2004).
  - [24] W.A. Gardner, *Introduction to random processes* (McGraw Hill, New York, 1990).
  - [25] S.M. Rochester and D. Budker, J. Mod. Opt. **49**, 2543 (2002).